Environmental Technology & Innovation 32 (2023) 103350

Contents lists available at ScienceDirect

Environmental Technology & Innovation

journal homepage: www.elsevier.com/locate/eti

Photocatalytic and adsorption performance of MXene@Ag/cryogel composites for sulfamethoxazole and mercury removal from water matrices

Harry K. Megbenu [a], Chingis Daulbayev [b,c], Armanbek Nursharip [b], Zhandos Tauanov [d], Stavros Poulopoulos [a], Rosa Busquets [e], Alzhan Baimenov [b,d,*]

[a] Department of Chemical and Materials Engineering, School of Engineering and Digital Sciences, Nazarbayev University, 53 Kabanbay batyr ave., 010000, Astana, Kazakhstan
[b] National Laboratory Astana, Nazarbayev University, 53 Kabanbay batyr ave., 010000, Astana, Kazakhstan
[c] Institute of Nuclear Physics, 1 Ibragimov st., 050032, Almaty, Kazakhstan
[d] Al Farabi Kazakh National University, 71 al-Farabi ave., 050040, Almaty, Kazakhstan
[e] School of Life Sciences, Pharmacy and Chemistry, Kingston University, Penrhyn road, KT1 2EE, Kingston upon Thames, Greater London, UK

ARTICLE INFO

Article history:
Received 7 July 2023
Received in revised form 14 August 2023
Accepted 22 August 2023
Available online 25 August 2023

Keywords:
Nanocarbon
Nanomaterial
Water filter
Emerging contaminant
Heavy metal

ABSTRACT

Water reuse is expected to grow with the increase of freshwater scarcity that is on the rise globally because of climate change. This research has addressed the preparation of an advanced material that can treat both inorganic and organic contaminants from water thanks to the synergy of its different components. Specifically, the advanced material is a novel hybrid filter media composed of a macroporous cryogel and single-layer $Ti_3C_2T_x$ MXene nanosheets modified with silver nanoparticles (AgNPs). The cryogel was prepared using polyethylenimine and dimethylacrylamide below subfreezing temperatures. Single-layer MXenes produced *via* etching of Al from Ti_3AlC_2 flakes were sorbed to the cryogel. AgNPs were prepared in-situ and deposited onto the MXenes. The composite was studied using SEM-EDS, TEM, XRD, XRF, FT-IR, zeta potential, DRS and it tested with two model substances that are global pollutants of distinct nature: the antibiotic sulfamethoxazole, that results from incomplete wastewater treatment, and Hg^{2+} from geogenic or industrial emissions. The composite acted as sorbent/photocatalyst and was highly effective towards the degradation of sulfamethoxazole under light irradiation together with adsorption of Hg^{2+} from waters, including river water. The photocatalytic activity of AgNP was enhanced by the MXene co-catalyst, while the cryogel served as scaffold for MXene@Ag and as Hg adsorbent. The effectiveness of composites reached 97% of degradation of sulfamethoxazole and around 98% of Hg^{2+} when working at concentrations greater than environmental levels. Hence, the combination of adsorption and photocatalytic properties in water filtration media consisting of MXene@Ag/cryogel composites and opportunity to explore for treating water.

1. Introduction

The increasing demand for freshwater resources is one the biggest challenges worldwide (Bruno et al., 2021). Wastewater treatment and recycling water will be major needs in the near future (Parvulescu et al., 2022). There is

* Corresponding author at: National Laboratory Astana, Nazarbayev University, 53 Kabanbay batyr ave., 010000, Astana, Kazakhstan.
E-mail addresses: r.busquets@kingston.ac.uk (R. Busquets), alzhan.baimenov@nu.edu.kz (A. Baimenov).

https://doi.org/10.1016/j.eti.2023.103350

worldwide concern regarding the presence of heavy metals and pharmaceutical products in wastewater as they are a threat to the natural ecosystem and human health (Aftab et al., 2023; Kwon et al., 2020). If untreated wastewater was used for the irrigation of crops, drinking or cooking, potentially because of water scarcity, the contaminants in wastewater would threaten the consumers' health (Aftab et al., 2023).

Mercury (Hg) is a highly toxic and persistent heavy metal that is more challenging to eliminate from water compared to other heavy metals (Ghosh et al., 2022). Efforts to reduce Hg emissions are supported by The UNEP Global Legally Binding Treaty on Mercury (Minamata Convention) (Kwon et al., 2020). The World Health Organization evaluated the risk of exposure to several forms of Hg from the consumption of drinking water and concluded that Hg^{2+} is the main form in drinking water (World Health Organization, 2013). Hg and its compounds are classed as a priority substances in the Water Framework Directive under the Environmental Quality Standards Directive; Directive 2008/105/EC amended by Directive 2013/39/EU.

Pharmaceutical products, especially antibiotics, are emerging pollutants found in the aquatic environment (Yang et al., 2017b). Their incomplete metabolism, and removal in wastewater treatment plants, contribute to their persistence and bioaccumulation (Hu et al., 2023). Sulfamethoxazole (SMX) is a commonly detected antibiotic in ground and surface water (Karimi et al., 2023).

Conventional treatments for heavy metal removal include electrochemical processes, precipitation, and ion exchange. These treatments present limitations such as high costs when scaling up (Amiri et al., 2016; Yadav et al., 2016; Zhou et al., 2014). Adsorption, on the other hand, has interest due to its simplicity and potential for low-cost treatment. Various materials, including polymers and inorganic sorbents, have been tested as adsorbents for Hg^{2+} removal (Baimenov et al., 2020). However, efficient methods for removing both organic and inorganic pollutants from water remain a challenge. Cryogels are synthetic 3D macroporous polymers with interconnected pores that are used for water filtration (Baimenov et al., 2022; Demirci and Sahiner, 2022; Dzhardimalieva et al., 2020). Their mechanism of removing ionic pollutants is similar to that of ion exchange resins, utilizing electrostatic forces (Lozinsky, 2002). Cryogels can be prepared from a wide range of monomers, and they provide functional groups that can be further modified, or adjusted to host nanoparticles, to improve their water treatment performance.

The application of photocatalysis, an advanced oxidation processes (AOP), in combination with adsorption, is used in the production of drinking water, and with less frequency, to treat wastewater. This is because of the lower concentration of suspended solids that drinking water has (which would block the light if present) and the greater cost that the production drinking water can assume. Even though adsorption and photocatalysis are separate processes, they can act synergistically in combination, resulting in enhanced water purification (Chen et al., 2017; Perera et al., 2022; Sheng et al., 2019). 2D Nanomaterials, such as MXenes, have favorable properties for water treatment applications because they have high photochemical stability and visible light response (Alhabeb et al., 2017; Deng et al., 2017). In particular, $Ti_3C_2T_x$ MXenes, exhibit high catalytic performance (Natu et al., 2019; Wu et al., 2020). Indeed, some MXenes have shown efficacy in removing heavy metal and antibiotics (Anasori et al., 2017; Li et al., 2021). Furthermore, the removal of the metal layer from the MXene precursor, MAX phase, generates ion exchange sites and favors the deposition of metal nanoparticles. These nanoparticles onto the carbon nanomaterial further improve electron transfer efficiency, where MXene acts as co-catalyst in the photocatalytic decomposition of organic pollutants.

The powder form of MXenes does not make them ideal for water treatment applications. In contrast, MXene immobilized in 3D polymeric scaffolds is a system with enhanced purification properties as opposed to both components acting separately. There are only a few studies that reported the application of MXene combined with porous polymers for water purification. Shahzad et al. synthesized $Ti_3C_2T_x$-sodium alginate core–shell spheres for the removal of mercury ions (Shahzad et al., 2019). The unique structure and developed surface area of spheres in combination with oxygenated functional groups of MXene enhanced Hg^{2+} adsorption with maximum removal capacity of 933 mg/g. In another work, Dong et al. prepared $Ti_3C_2T_x$/alginate composites for Pb^{2+} and Cu^{2+} removal, where the maximum removal capacity reached 383 and 88 mg/g, respectively (Dong et al., 2019). The modification of tannic acid/cellulose aerogels with ZIF-67/$Ti_3C_2T_x$ was used for the photocatalytic degradation of tetrabrombisphenol A under visible light (Wang et al., 2022). The ZIF-67/$Ti_3C_2T_x$ heterojunction on aerogel contributed to the removal of up to 99.8% of tetrabrombisphenol A. Li et al. applied Cu@$Ti_3C_2T_x$-polyacrylamide hydrogel for the fast reduction of 4-nitrophenol to 4-aminophenol in aqueous solution (Li et al., 2022). Almost 100% of 4-nitrophenol was transformed into 4-aminophenol within 4 min. In our study, a composite material comprising MXene@Ag/cryogel was developed for the simultaneous adsorption of metal and degradation of organic contaminants from water, and mechanisms underlying the removal of the pollutants are proposed. The removal of contaminants of such different chemical nature has not been addressed in other works and opens the door to composites offering multipurpose treatment of effluents from hazardous contaminants.

2. Materials and methods

2.1. Materials

Cryogels were prepared with dimethylacrylamide (DMAAm, 99%), *N, N′*-methylenebisacrylamide (BisAAm, 99%), polyethylenimine (PEI, 99%), *N, N, N′, N′*-tetramethyl ethylene diamine (TEMED, 99%), allylamine (98%), phosphoric acid (H_3PO_4, ≥85%), sodium hydroxide (NaOH, ≥98%) and ammonium persulfate (APS, 98%), all from Merck. Hydrochloric

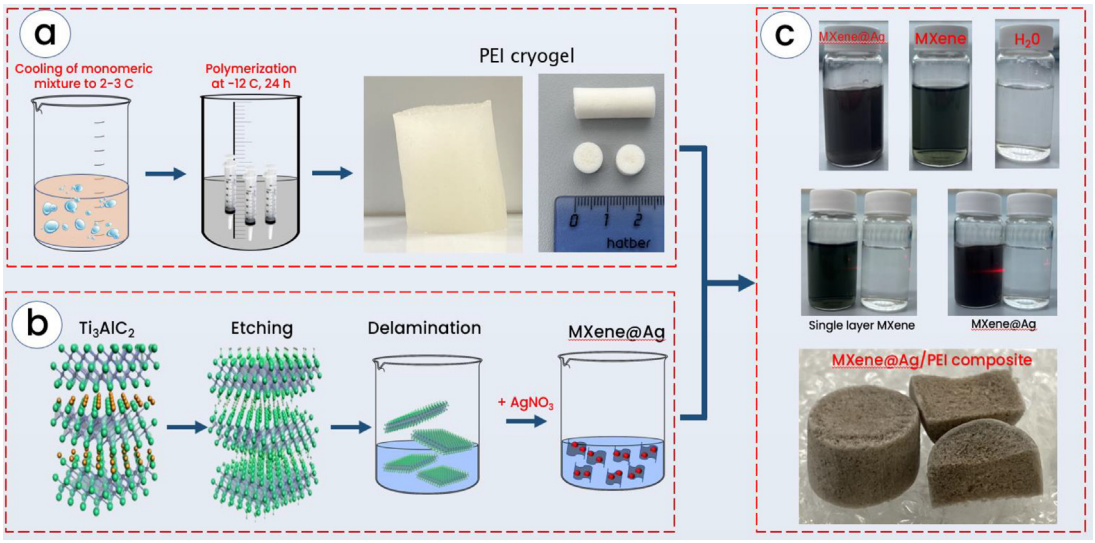

Fig. 1. Cryogel (a), MXene@Ag (b), and composites (c) synthesis process scheme.

acid (HCl, 37%), hydrofluoric acid (HF, ≥48%), mercury (II) chloride ($HgCl_2$, ≥99.5%), lithium chloride (LiCl, ≥99%), silver nitrate ($AgNO_3$, >99%) and sulfamethoxazole (SMX) were purchased from Merck (Germany). Ti_3AlC_2 MAX phase (99%) was purchased from Carbon-Ukraine LTD. All experiments were performed on DI water (Puris Eco RO 1600-M, South Korea).

2.2. Synthesis of PEI cryogels

Free radical polymerization was used for the synthesis of cryogels. Details of the synthesis route are shown in Fig. 1a. Allylamine and PEI were the main monomers; TEMED and APS were the initiator and catalyzer respectively; BisAAm was the crosslinker; and DMAAm was the precursor of the amide functional group. Approximately 20 mL of water was degassed *via* purging N_2 gas and it was split into two beakers. In one of them, of BisAAm (0.26 g) and of PEI (0.25 g) were slowly added to the degassed water (10 mL) under stirring. Allylamine (0.3 mL) was added to the second beaker with 8.5 mL of water. This was followed by the addition of 0.24 mL 85% H_3PO_4. Here, the pH was regulated between 7 and 8 by the addition of 5M NaOH. TEMED (0.02 mL) was then added, and the mixture was placed in an ice bath for 40 min to reach ∼2–3 °C. APS (5%, 0.80 mL) was added to the solution, and it was quickly transferred into test tubes immersed in ethanol (−12 °C) in beakers kept in the cryostat (Julabo F34) also containing ethanol at −12 °C. The polymerization took place for 24 h at −12 °C. The cryogel monoliths were then washed in water several times, freeze-dried and preserved for future use.

2.3. Preparation of MXene

Ti_3AlC_2 (1 g) MAX phase was gently dispersed in 20 mL of etchant by ratio 6:3:1 (v/v) of HCl, water, and HF respectively and stirred for 24 h at 35 °C in a slightly capped polyethylene container as reported elsewhere (Mathis et al., 2021) (Fig. 1b). The etched MXene was washed via repeated centrifugation-decantation at 3500 rpm until a pH of approximately 6–7 was obtained. In the delamination process, 0.5 M LiCl solution (50 mL) was prepared and mixed with the obtained MXene suspension and stirred for 5 h at room temperature. The LiCl/MXene suspension was centrifuged at 3500 rpm for 5 min to remove residual LiCl. The MXene sediment was repeatedly washed at 3500 rpm in water (180 mL) for 5 min. The third wash cycle is the key step where the MXene solution (180 mL) was centrifuged for 1 h at 3500 rpm and the single layer MXene suspension was collected. The latter procedure was reiterated for additional 4 cycles and freshly collected MXene was immediately used for modification experiments.

2.4. Synthesis of MXene@Ag composites

The as-synthesized MXene colloidal suspension (200 mL) was mixed with 30 mL of a solution of $AgNO_3$. Tests were carried out where such solution was prepared by dissolving 100, 150 and 200 mg of $AgNO_3$. These individual solutions were stirred for 10 min at 300 rpm. Depending on the mass of $AgNO_3$ the MXene@Ag samples were labeled as $MXene@Ag_{100}$, $MXene@Ag_{150}$, and $MXene@Ag_{200}$. After mixing, the solutions were washed through centrifugation/decantation for 5 min at 3500 rpm in 96% ethanol. The washing was carried out three times. The solid residue was collected with 0.45 μm PVDF

filter paper (Milli-Q, USA), vacuum dried for 24 h, and the MXene@Ag flakes were obtained and kept for further analysis. For the modification of the cryogel, freshly prepared MXene@Ag colloidal solutions were used without drying. Photos of single-layer MXene and MXene@Ag colloidal solutions are shown in Fig. 1c.

2.5. Cryogel modification process

Cryogel monoliths (20 mg) were immersed in 10 mL of MXene@Ag colloidal solution and left shaking (120 rpm) for 24 h for the incorporation of MXene@Ag into the cryogel structure. The prepared cryogels were washed with water to remove any MXene@Ag residues from the cryogel pores. The modified composites were lyophilized using a Labconco freeze dryer and stored in sealed container.

2.6. Materials characterization

To determine the presence of various functional groups within the structure of the synthesized materials, a Cary 600 Series FTIR spectrophotometer (Agilent Technologies) equipped with an ATR module infrared spectrum was used. The spectra were recorded within the range of 4000–400 cm^{-1} with resolution of 4 cm^{-1} and a scanning speed of 1 cm^{-1} s^{-1}. The synthesized samples were lyophilized and ground with a mortar into a fine powder before its analysis with IR. Scanning Electron Microscope (SEM) (Zeiss Crossbeam 540, Germany) operating at 5–20 kV was used for the characterization of the morphological structure of the materials. The elemental analysis of bare and modified composites was done with an energy dispersive X-ray (EDX) spectrometer (INCA X-Sight, Oxford Instruments) connected to the SEM. The size and structure of composites were studied using a high-resolution transmission electron microscope (TEM) (JEM-2100 LaB6 HRTEM, JEOL, Japan) operating at 80 kV. To determine the presence and structure of $Ti_3C_2T_x$ and Ag in pure form and in the modified cryogels, pre-ground powdered samples were suspended in ethanol and sonicated to prevent the agglomeration of dispersed particles. An aliquot of the suspended composite (10 μL) was dropped onto a 300-mesh carbon-coated copper grid and dried overnight. Data on the phase composition of the initial $Ti_3C_2T_x$ and modified cryogel composites were obtained by X-ray diffraction (XRD). XRD analysis of the composites was carried out using an X-ray diffractometer (Rigaku SmartLab, Japan) with a HyPix-3000 high-energy resolution 2D HPAD detector. The scanning range was from 5 to 70°, with a diffraction angle of 2θ, at 40 kV and 40 mA. X-ray Photoelectron Spectroscopy (XPS) was carried out with the model VG-Microtech Mutilab 3000 (UK), equipped with CLAM 4 hemispherical electron analyzer and Al/Mg X-ray radiation twin source to determine the chemical composition of materials' surface. The binding energies (BE) were calibrated according to the signal C1s core level being at 284.8 eV as a reference. Light transmission and reflection measurements of the obtained photocatalysts were carried out on a Shimadzu UV-3600 spectrophotometer. UV–Vis diffuse reflectance spectra (UV–Vis DRS) was collected within the range between 200–800 nm using the Perkin Elmer Lambda 35 spectrophotometer at 4.0 nm spectral bandwidth with a scan rate of 400 nm/min. The recorded spectral data interval was set at 1.0 nm. The $BaSO_4$ bulk was used as the reference standard.

2.7. Photocatalytic experiments

The photocatalytic experiments were done using an OCRS-V photochemical reactor (Toption Instruments, China) under 500 nm wavelength with xenon lamp powered at 300 W. The distance between the solution and lamp was 15 cm. All experiments were performed using quartz vessels with SMX concentrations from 5 to 50 mg/L, volume of 100–400 mL, pH 2–9 and mass loading of composites from 10 to 50 mg depending on the experimental conditions. Prior to photocatalysis experiments, there was a period of 30 min of adsorption in the dark to achieve adsorption–desorption equilibrium. The solution was magnetically stirred throughout the experiment. All photocatalytic experiments were carried out for 60 min and 1 mL aliquots were collected at selected time points, filtered using 0.45 μm PVDF syringe filter, and analyzed by UV–Vis to monitor the degradation of SMX in water. Experiments were performed in duplicate and the average values with standard deviation were plotted. The river water used for experiments was collected from the Ishim river (coordinates 51.109729°, 71.449968°), Astana, Kazakhstan, and was filtered with a paper filter (Whatman Grade 1) prior to use.

2.8. Mercury adsorption experiments

The performance of the synthesized materials for Hg^{2+} adsorption was determined using a mercury analyzer (Lumex RA-915M, Russia). The adsorption process was performed in quartz beakers at room temperature. The adsorption experiment was carried out in two separate solutions: in one, there was a SMX (10–30 mg/L) and $HgCl_2$ mixture (5–20 mg/L); and in a second one, there was only $HgCl_2$ in solution (5–20 mg/L), where concentrated HCl was used to adjust the pH. Hg removal from the SMX-$HgCl_2$ mixture was measured with the OCRS-V photochemical reactor according to the procedure described in Section 2.7. Depending on the experiment, between 10 and 40 mg of cryogel and/or its composites were dispersed in 100–400 mL $HgCl_2$ solution (5–30 mg/L) and left under stirring for 90 min under light irradiation or in dark conditions. Every 10 min, 30 μL of sample was collected and analyzed on Lumex RA-915M to record the residual concentration of mercury. All experiments were performed in duplicate and the average values with error bars (corresponding to the standard deviation) are presented in Figs. 7–8. The speciation of mercury ions depending on the pH for 10 mg/L $HgCl_2$ solution was obtained using Visual MINTEQ 3.1 program.

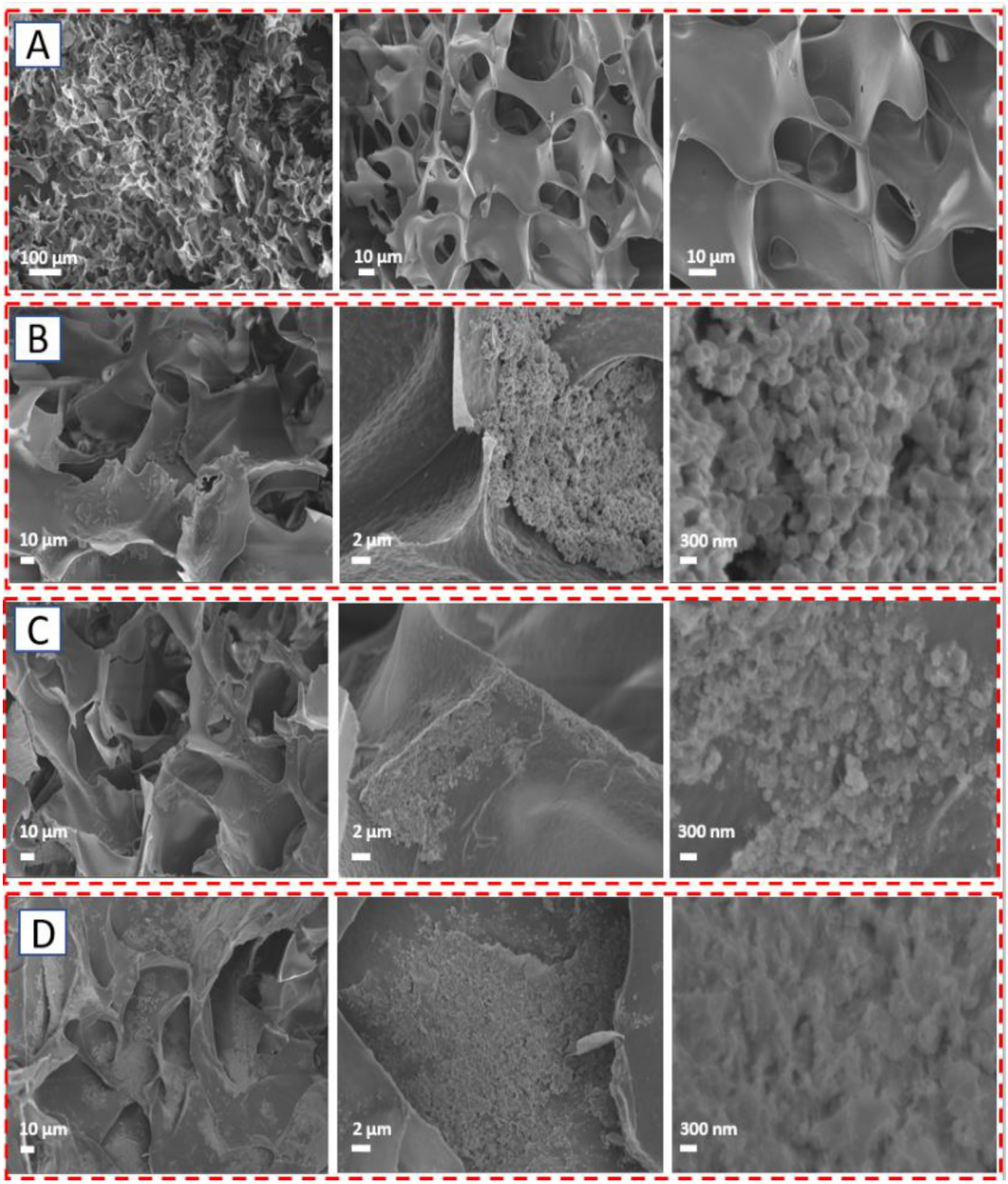

Fig. 2. SEM micrographs of (A) PEI cryogel, (B) MXene@Ag_{100}/PEI, (C) MXene@Ag_{150}/PEI, (D) MXene@Ag_{200}/PEI at different magnifications.

3. Results and discussion

3.1. Characterization

PEI cryogels had highly interconnected macroporous structure with smooth walls. The pore size ranged 10–80 µm. Representative domains of the cryogel with different magnifications are shown in Fig. 2a. Such structure facilitates the flow of water within the pores. In the case of composites MXene@Ag_{100}/PEI, MXene@Ag_{150}/PEI and MXene@Ag_{200}/PEI, the superior macroporous structure of the cryogel could still observed, however great part of the surface was covered with MXene@Ag particles (Fig. 2b–d). The modification of MXene with Ag on surface of PEI cryogel was confirmed by EDX mapping (Supplementary materials Fig. S1-S3). The mass loading of Ag on MXene influenced the distribution

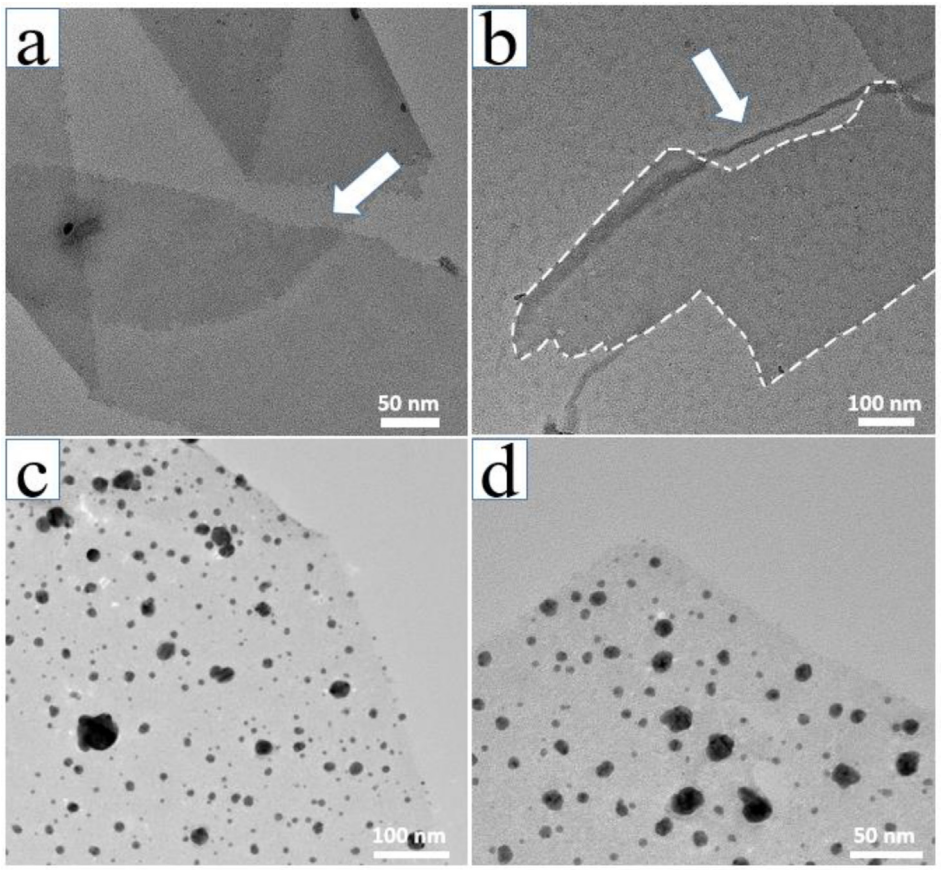

Fig. 3. TEM images of MXene (a, b) and MXene@Ag (c, d) at different magnifications, where the opaque dots correspond to Ag nanoparticles.

of nanoparticles, with greater formation of aggregated particles on the surface of the cryogel composites with greater starting mass of $AgNO_3$. Among the composites with different Ag loadings, MXene@Ag_{100}/PEI showed less aggregation of MXene@Ag, while MXene@Ag_{150}/PEI and MXene@Ag_{200}/PEI presented a thick layer of particles onto the cryogel. According to the EDX mapping analysis, the silver content in the MXene@Ag_{100}/PEI, MXene@Ag_{150}/PEI and MXene@Ag_{200}/PEI was 16.6, 29.8 and 34.2 in mass (%), respectively (Supplementary Fig. S1-S3).

The surface morphology of the as-prepared single-layered MXene and MXene@Ag_{100} samples was studied with TEM. Single layer MXene flakes with diameter of 2–3 μm are shown in micrograph Fig. 3a,b (pointed by an arrow). Detail of internal morphology of the synthesized MXene@Ag is shown in Fig. 3c, d: the sizes of the observed AgNPs on the MXene flake surface varied from ∼3 to 20 nm. An increase in the concentration of $AgNO_3$ led to an increase in distribution and possible aggregation of the resulting an increase in AgNP particles size.

The XRD analysis was performed before and after the modification of the cryogels (Fig. 4a) to study the crystalline structure of the AgNPs deposited on MXenes. Similar patterns were present from all samples except from the PEI cryogels that did not have MXenes where no sharp peaks of the crystalline structure were observed due to the amorphous nature of the polymer. Intense peaks corresponding to AgNPs were observed on the lattices (111), (200), (220), and (311) confirming the successful synthesis of MXene@Ag composites (Zou et al., 2016). Three small peaks at $2\theta \approx 6.18°$, 27.88° and 32.29° respectively correspond to the (002), (004), and (006) lattice planes of $Ti_3C_2T_x$. The same pattern of XRD peaks was observed for unmodified MXene, and MXene@Ag (included in Fig. S4). The greater the silver concentration used during the synthesis of composites, the more intense their corresponding peaks appeared with respect to the peaks corresponding to the MXenes.

The functional groups of the synthesized PEI cryogels and their composites were analyzed by FT-IR and are presented in Fig. 4b. The FT-IR spectra of all materials have a similar pattern, although their band intensity differs: higher intensities were observed for the composites as compared with the cryogel on its own. A main band of MXene is at ∼3300 cm^{-1} corresponds to O–H stretching vibrations of –OH functional groups in $Ti_3C_2T_x$. The intensity of O–H peaks decreased in such order MXene@Ag_{100}/PEI > MXene@Ag_{150}/PEI > MXene@Ag_{200}/PEI due to the increased concentration of AgNPs on the MXene, where Ag^+ ions were exchanged with H^+ of –OH–$Ti_3C_2T_x$. The C–H stretching bands were observed at 2927 cm^{-1} and 2853 cm^{-1} in all materials. The peak at 1618 cm^{-1} (N–H bending) denoted the presence of an amide group

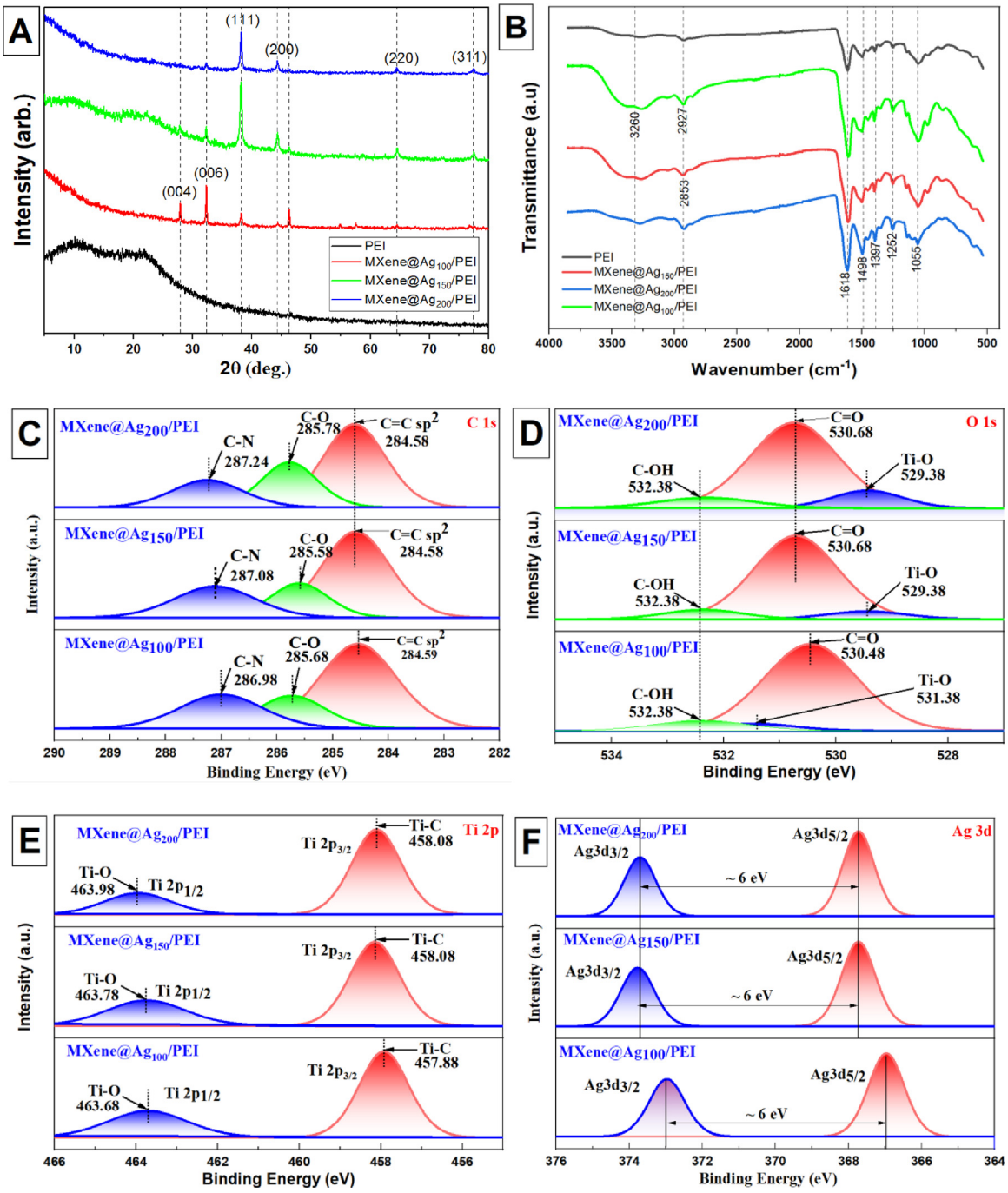

Fig. 4. XRD spectra (a), FT-IR spectra (b), and XPS spectra for C (c), O (d), Ti (e), and Ag (f) for the synthesized composites.

in the composite since *N,N*-dimethylacrylamide is one of the major precursors used in the cryogel synthesis. There were prominent peaks at 1055 cm^{-1} and 1112 cm^{-1} that were assigned to O–H bending and C–O stretching bonds (Demirci and Sahiner, 2022). Characteristic imide groups are exhibited at 1618 cm^{-1} for C–N bending. An O–H bending of carboxylic acid group shows an absorption peak at 1397 cm^{-1}.

Characteristic C 1s, O 1s, Ti 2p, and Ag 3d bands in MXene@Ag_{100}/PEI, MXene@Ag_{150}/PEI, and MXene@Ag_{200}/PEI are shown Fig. 4c–f. The C 1s region (Fig. 4c) was fit with three peaks and their binding energies (BEs) fell within 287 to 285 eV. Here, the most prominent peak had a BE of 284 eV which corresponds to C–C while the other two peaks may correspond to C–O and C–N bonds as reported by other works (Choi et al., 2018; Halim et al., 2016). The three additional

asymmetric peaks for C 1s with BEs 285, 286, and 287 eV are considered to emerge from the conjunction bonding with adjacent N atoms in PEI (Choi et al., 2018). For the O 1s region (Fig. 4d), three peaks were observed to overlap, and the most prominent peak had BE corresponding to O atoms near vacant sites in TiO_2 at 531 eV. The main peak of O 1s at 530 eV can be attributed to C=O. The peaks with BEs of 532 eV denote O–H groups (Halim et al., 2016). Water adsorption on the titania surface provides a peak at 533.5 eV. From Fig. 4e, the presence of Ti 2p from the XPS spectra shows the contribution of C and O mainly comes from Ti–C and Ti–O respectively. However, the peaks at 457.88 eV and 463.78 eV respectively denote sp^3 and sp^1 hybridization which is a contribution from Ti–C and Ti–O MXene bonds (Satheeshkumar et al., 2016). Overall, the BEs obtained for the synthesized MXene-containing composite was higher than the (BE reported for the precursor Ti_3AlC_2 MAX phase (Halim et al., 2016). This narrow shift is due to Al layers replacement by more electronegative groups such as –F, –O, and –OH. 3D core levels of Ag (Fig. 4f) with chemically distinguished spin–orbit pairs were obtained at 368.8 eV and 373.6 eV for Ag $3d_{5/2}$ and $3d_{3/2}$ respectively. A characteristic peak for electron emission from Ag atoms gives ∼6 eV as the difference in BE from the component with low binding energy (368.8 eV).

The diffuse reflectance spectra (DRS) in the ultraviolet and visible ranges for the obtained samples is shown in Fig. S5a. All samples presented a pronounced reflection peak at 340 nm. At the same time, there are distinct absorption peaks in the region ∼380 nm, which were shifted towards low energy wavelengths in the composites. Fig. 6b shows the Kubelka–Munk plots used to determine the band gaps for the obtained samples. The band gap was determined from the Eq. (1):

$$(\alpha h\nu)^n = A(h\upsilon - E_g) \tag{1}$$

where α is absorption coefficient, A and h are proportional and Planck's constant respectively, ν is light frequency and E_g is the band gap. The n value depends on the type of optical transition in a semiconductor, where n = 2 for direct transition and $n = 1/2$ is for indirect transition. According to the plot of $\alpha h\nu^{1/2}$ versus eV (Fig. S5b), the band gap was determined as 2.28 eV for MXene@Ag_{100}/PEI; 2.36 eV for MXene@Ag_{150}/PEI; and 2.46 eV for MXene@Ag_{200}/PEI composites. These results suggest that the lower the concentration of AgNPs deposited on MXene@Ag hybrids, the lower the band gap energy is due to surface plasmon resonance effect of AgNPs and metallic properties of $Ti_3C_2T_x$. This indicates that the presence of MXene@Ag in the sample makes it possible to absorb radiation with low energy values (Udayachandran Thampy et al., 2019).

The influence of pH on the surface charge of materials was analyzed using Zetasizer within the pH range from 2 to 9 and presented in Fig. S6. All synthesized materials presented positive zeta potential. Such positive charge could be attributed to PEI which is a cationic polyelectrolyte (Zhang et al., 2021b). The amino groups of PEI and allylamine may be protonated in solution causing the surface charge to be highly positive and capable of adsorbing negatively charged pollutants in solution. The PEI cryogels and their composites showed a similar trend in all studied pH conditions where the zeta potential value decreased from 32 to 5 mV. A highly positive zeta potential value was observed within pH 3–4 where the cryogel surface was more protonated. The PEI composite and MXene@Ag_{100}/PEI presented zeta potential of 15 mV at pH 2, and ∼32 mV at pH 3. Zeta potential values started to decrease exponentially with pH increase in both samples. MXene@Ag_{150}/PEI and MXene@Ag_{200}/PEI cryogel composites had zeta potential of 25 mV and 30 mV, respectively. According to research conducted by Szuplewsa et al., the zeta potential for 2D Ti_3C_2 after HF etching was negative(Szuplewska et al., 2019). Therefore, the positive zeta potential values obtained for the synthesized composites could be due to the PEI cryogel being highly positive.

3.2. Removal performance

3.2.1. Influence of composites loading, pH, volume, and concentration of SMX on its photocatalytic degradation

The photodegradation of SMX could be affected by the pH of the solution, hence it was investigated at pH 2–9 (Oliveira et al., 2019). SMX is an acidic molecule with $pK_{a1} = 1.6$ and $pK_{a2} = 5.7$ and the protonation state of SMX plays a significant role in photolysis (Zhou et al., 2015). Our results (Fig. 5a) found that acidic conditions were favorable for the photodegradation of SMX while basic conditions lead to poor degradation, which corresponds to previous results reported elsewhere (Zhou et al., 2015). Above pH 5, the degradation of SMX decreased. The best SMX degradation performance (51%–58%) by MXene@Ag/PEI composites was found to be at acidic conditions (pH 2–4) with an initial SMX concentration and composites dosage of 20 mg/L and 10 mg, respectively. The optimal pH that led to the highest removal efficiency of SMX was pH 3. Hence, further experiments on SMX photocatalysis were conducted at pH 3.

Treating water (100, 200 and 400 mL) contaminated with 30 mg/L SMX under photocatalysis conditions in batch mode using 10 mg of MXene@Ag/PEI composites (Fig. 5b) led to all composites degrading 50%–52% from SMX from 100 mL and 200 mL 30 mg/L solutions without a noticeable effect of the Ag amount. In contrast, 59% of SMX (400 mL of 30 mg SMX/L) was degraded with MXene@Ag_{100}/PEI followed by MXene@Ag_{200}/PEI (54%) and MXene@Ag_{150}/PEI (51%). It is interesting to note that MXene@Ag_{150}/PEI and MXene@Ag_{200}/PEI revealed a similar performance across all volumes under study with an average degradation amount of 51%.

Tests carried out with different mass of composite (10, 50 and 100 mg) (Fig. 5c) showed the highest degradation of SMX (59%) with 10 mg and 50 mg MXene@Ag_{100}/PEI, while the lowest catalytic performance was obtained for 100 mg MXene@Ag_{200}/PEI. This may be because the high density of positive charge of the composites may be hindering positively charged SMX molecules to approach the surface. There was also a negative trend for SMX degradation with an increase

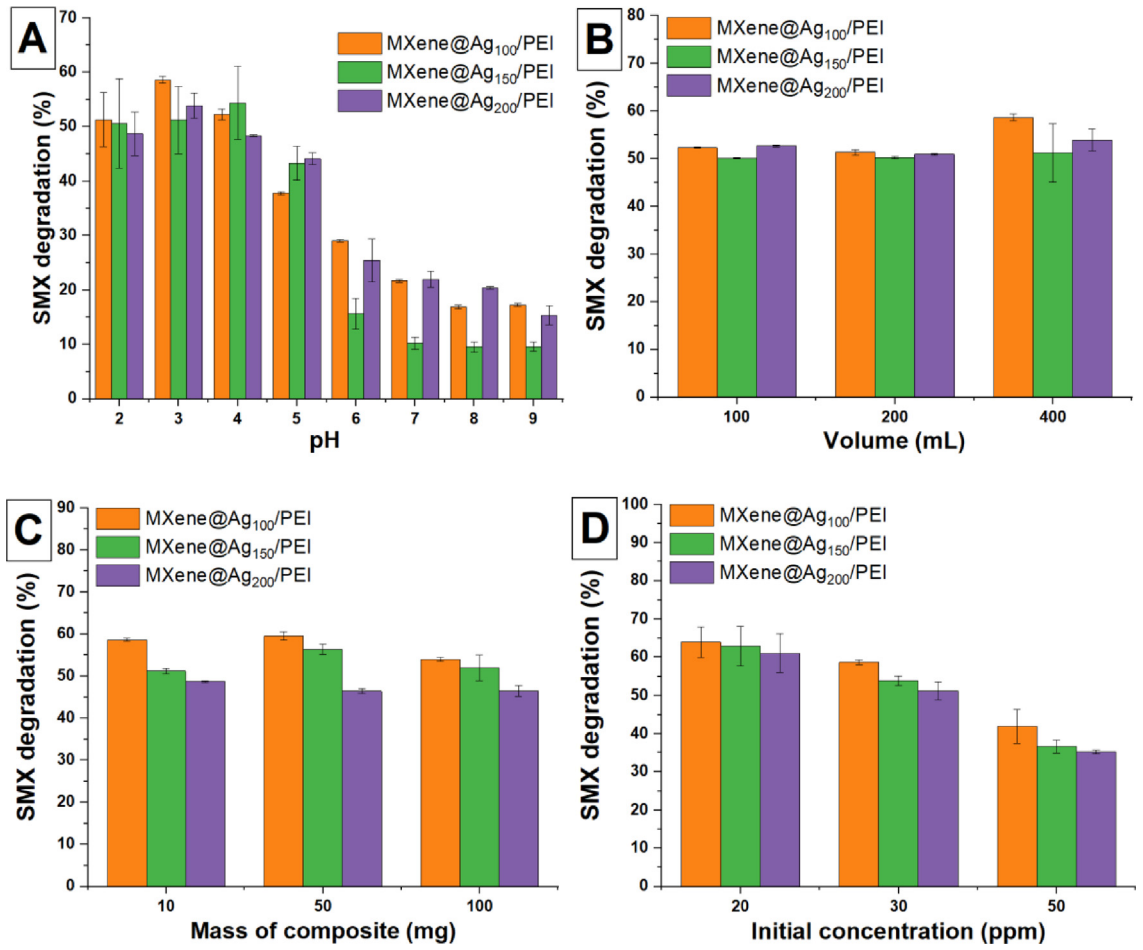

Fig. 5. Effect of various parameters relevant in the photocatalytic degradation of SMX by MXene@Ag/PEI composites : (a) pH, (b) volume of 30 mg/L of SMX solution, pH3, (c) different loading of MXene@Ag/PEI composites per 100 mL 30 mg/L of SMX, pH3, and (d) SMX starting concentration in 100 mL spiked water, pH3. The error bars correspond to the standard deviation of n = 2.

of Ag amount in MXene@Ag/PEI composites (Fig. 5c, d). This is possibly due to the aggregation of Ag nanoparticles and partial blockage of MXene surface by AgNPs.

In the experiments on different initial concentrations of SMX (20, 30 and 50 mg/L) (Fig. 5d) the increase of the initial concentration of SMX strongly affects the degradation profile. For example, MXene@Ag_{100}/PEI, MXene@Ag_{150}/PEI, and MXene@Ag_{200}/PEI degraded 61%–63% of 20 mg/L SMX solutions. In contrast, the studies on 30 mg/L and 50 mg/L of SMX showed less degradation of the antibiotic, but followed the same trend regarding the performance of the composite: MXene@Ag_{100}/PEI > MXene@Ag_{150}/PEI > MXene@Ag_{200}/PEI. Similar photocatalytic performance was recorded for a 2D-composite of rGO/Cu_2O that showed 50% degradation of SMX with an initial concentration of 5 mg/L (Liu et al., 2016). Another study conducted on metallic Ag and TiO_2 nanoparticles co-doped composite ($H_3PW_{12}O_{40}$/Ag–TiO_2) showed 51.3% degradation of SMX from aqueous solution of SMX at 40 mg/L after 2 h of irradiation with visible light (Xu et al., 2012). The high solubility of SMX, and proximity to the catalyst, may be the factors associated with its limited degradation in photocatalytic composites.

3.2.2. Adsorption of mercury

To evaluate the adsorption properties of pristine (PEI) and Ag-modified cryogels (MXene@Ag_{100}/PEI, MXene@Ag_{150}/PEI, and MXene@Ag_{200}/PEI), 10 mg from each sorbent, separately, were used for the removal of Hg^{2+} from aqueous solution. Two different volumes (100 and 200 mL) and three different concentrations (5, 10 and 20 mg/L) were studied, the studies were carried out in batch mode as indicated in Section 2.8. According to the results, the pristine PEI cryogels displayed the lowest adsorption capacities in every case, which ranged from 22 to 39 mg Hg^{2+}/g for the 100 mL samples and 27.7 to 80.3 mg Hg^{2+}/g for 200 mL Hg solution, respectively (Fig. 6). The Ag-modified samples, on the other hand, had improved adsorption capacities. For example, the MXene@Ag_{200}/PEI reached 153.05 mg Hg^{2+}/g composite when incubated in batch mode within 100 mL 20 mg/L Hg solution (Fig. 6A), which is almost 4-fold higher in comparison to pristine

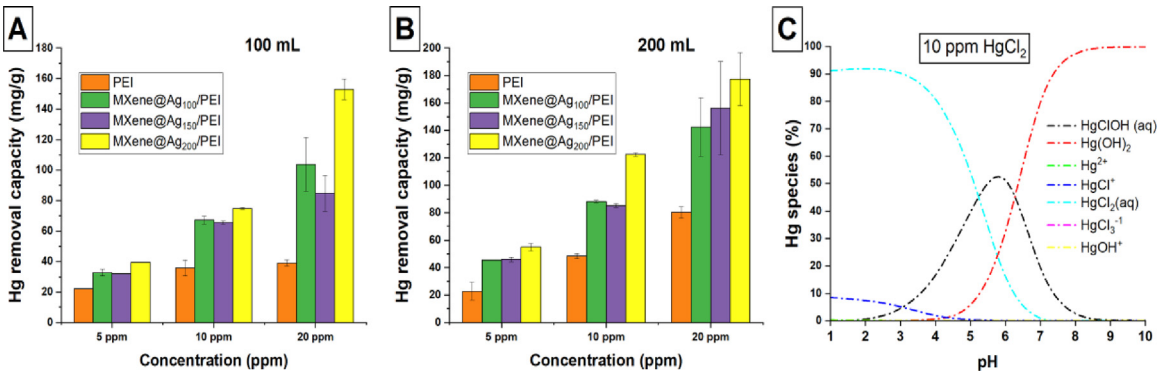

Fig. 6. Adsorption of mercury with different starting concentrations (x axis) from 100 (a) and 200 (b) mL solutions and (c) speciation diagram of 10 mg/L $HgCl_2$ as a function of pH obtained using Visual MINTEQ 3.1 program. The error bars correspond to the standard deviation of n = 2. The pH of the solution had been adjusted to 3 in A and B.

PEI (39 mg Hg $^{2+}$/g composite). It is interesting to note that MXene@Ag_{100}/PEI and MXene@Ag_{150}/PEI demonstrated comparable adsorption capacity values for 5 mg/L and 10 mg/L Hg^{2+-} solutions while showing somewhat difference for 20 mg/L Hg^{2+-}-solutions (103.65 mg/g and 84.8 mg/g, respectively) although the difference was not significant at p 0.05. Mercury removal studies from 200 mL spiked solutions under the mentioned concentrations also had a substantial increase in adsorption capacities for all Ag-modified composites and followed equivalent trends than what was observed with the 100 ml solutions in most cases (Fig. 6B). The highest adsorption capacities were observed for MXene@Ag_{200}/PEI which varied from 55 mg/g to 177.4 mg/g, whereas MXene@Ag_{150}/PEI and MXene@Ag_{100}/PEI showed comparable values with 5 mg/L and 10 mg/L Hg-solutions as in previous experiments. A clear difference between these two samples was recorded in adsorption experiments from 20 mg/L Hg-solution showing 142.5 mg/g for MXene@Ag_{100}/PEI and 156.2 mg/g for MXene@Ag_{150}/PEI. Pristine PEI samples displayed the lowest performance in all study conditions with adsorption capacities ranging between 27.7–80.3 mg/g. It should be noted that speciation fraction analysis of 10 mg/L $HgCl_2$ solution under different pH values was conducted to examine and quantify the existence of competing species that may hinder adsorption performance (Fig. 6C). According to these findings, between pH 1–4, $HgCl_2$ predominantly exists in the aqueous form with a fraction of $HgCl_{2\ (aq.)}$ reaching up to 92% under strongly acidic conditions. Between pH 4 to 7, other competing species of $HgCl_2$ such as $Hg(OH)_2$ and $HgClOH_{\ (aq.)}$ may co-exist with $Hg(OH)_2$ being predominant above pH 7. Similar studies on cross-linked PEI are in agreement with the findings of this research, wherein the removal efficiency from chloride and nitrate solutions of mercury reached 98% and 86%, respectively (Privar et al., 2018). Research on Hg^{2+} removal from water using rGO/PEI aerogels showed comparable adsorption capacity to the composites developed in this work, with 209 mg Hg/g composite (Borrás et al., 2022).

3.2.3. Influence of co-existing ions on SMX photocatalytic degradation

The photocatalytic degradation of SMX from the mixture of SMX and $HgCl_2$ in different water matrixes (water and river water) was carried out by using four different dosages of Ag-modified adsorbents under dark and light-on conditions (Fig. 7a–f). The use of SMX/$HgCl_2$ and river water was done to examine the influence of Hg cations and presence of co-existing ions on the SMX photodegradation efficiency. In general, the results of Ag-modified adsorbents in water showed that the degradation pattern of SMX did not depend on the adsorbent dosage, while the effect of UV irradiation played a key role in photocatalytic activity. After a 30-min kinetics run of Ag-modified samples under dark conditions, none of the adsorbents showed a noticeable removal or degradation of SMX, whereas between 30 to 90 min with a light-on condition, the C_t/C_0 of SMX reached almost 0.65 just in 10 min. The Ag-modified MXene@Ag_{100}/PEI, MXene@Ag_{150}/PEI, and MXene@Ag_{200}/PEI displayed similar results with negligible effect under dark conditions and profound changes under light-on conditions with the average lowest C_t/C_0 values of 0.2. All dosages showed comparable results within the standard deviation demonstrating a strong dependence on light irradiation rather than on adsorbent amount. The positive co-catalyst effect of the MXene quantum dots was determined in a composite that was used for the photodegradation of SMX and 4-chlorophenol (Saravanakumar et al., 2023). It was interpreted that MXene acted as an electron mediator as well as maintained strong redox stability within heterojunctions of composite that further enhanced photocatalytic activity (Saravanakumar et al., 2023). The kinetics of the photocatalytic degradation rate of SMX was determined using the Langmuir–Hinshelwood pseudo-first-order rate kinetics model using the Eq. (2):

$$-\ln\left(\frac{c_t}{c_0}\right) = k_{app}t \tag{2}$$

where, C_0 and C_t (mg/L) are the initial concentrations and at time t (min), and k_{app} (min^{-1}) is the apparent rate constant of the reaction that was calculated from the slope of ln (C_t/C_0) versus irradiation time t. The reaction rate constant presented

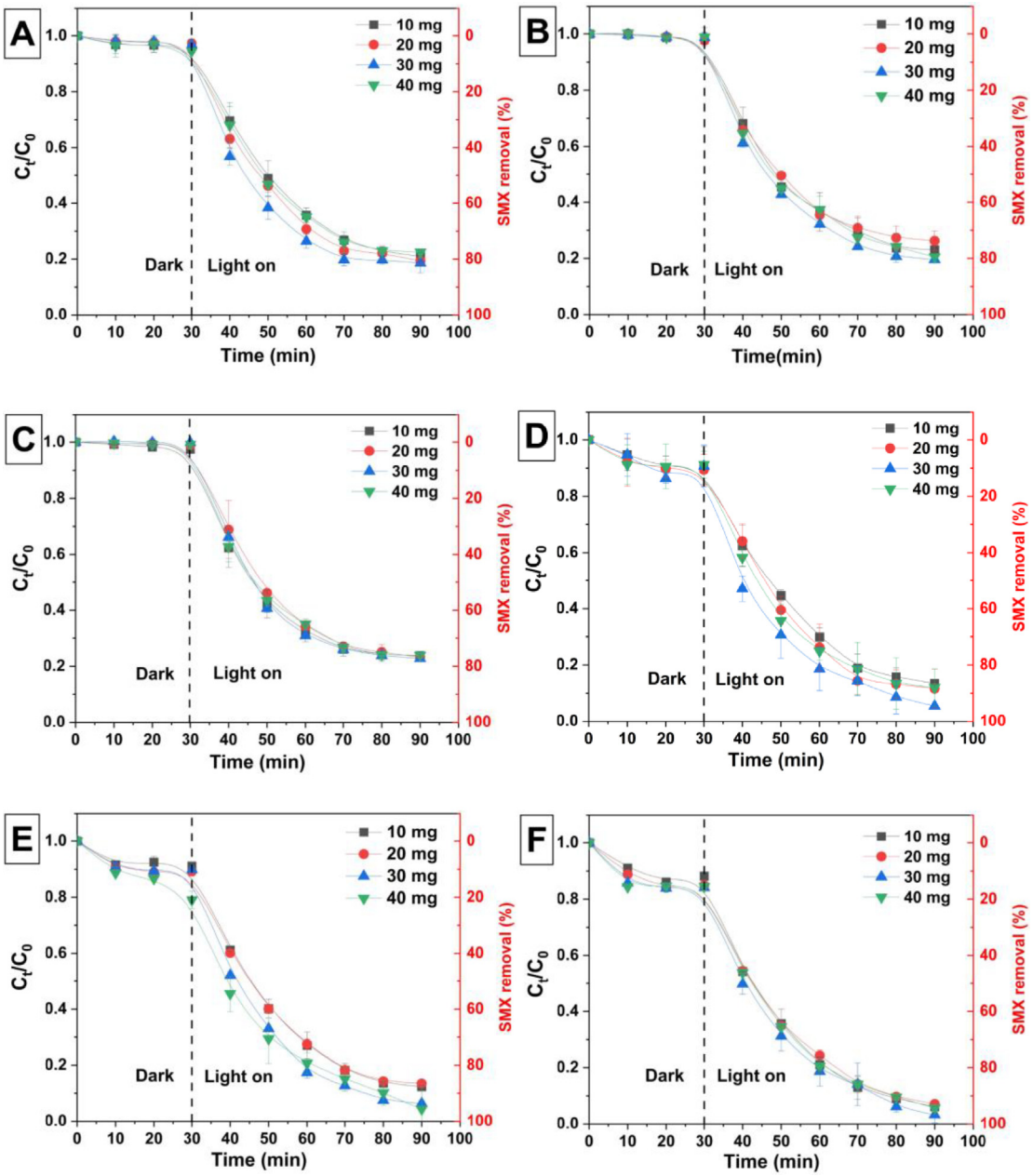

Fig. 7. Photocatalytic degradation of SMX with 10, 20, 30, 40 mg of MXene@Ag_{100}/PEI; MXene@Ag_{150}/PEI; and MXene@Ag_{200}/PEI from water (a, b, c) and river water (d, e, f).

in the Fig. S7a–f was calculated for all composites depending on the mass loading and the water matrix. It was found that k_{app} for MXene@Ag_{100}/PEI varied from 0.052 to 0.081 min^{-1} in water and 0.055–0.092 min^{-1} from river water. For MXene@Ag_{150}/PEI the k_{app} values were 0.058–0.072 min^{-1} and 0.072–0.099 min^{-1}, while for MXene@Ag_{200}/PEI were ranged from 0.056–0.068 and 0.056–0.07 min^{-1} for DI and river water, respectively.

The Ag-modified adsorbents were also studied using river water samples to evaluate the effect of photocatalysis on SMX degradation under conditions close to environmental conditions. In contrast to studies in DI water, all adsorbents showed a noticeable decrease of C_t/C_0 values on average up to 0.85 within a 30-min kinetics run under dark conditions. According to the IC analysis results (Table S1), the amount of cations in river water slightly decreased after the addition of SMX, which suggests the formation of ion pairs with SMX. Therefore, that phenomenon affected the adsorption of SMX under dark conditions in river water. During the light-on condition starting from the 30-min point, the MXene-Ag photocatalysts start to promote the gradual degradation of SMX that allowed it to reach C_t/C_0 values of 0.05, on average,

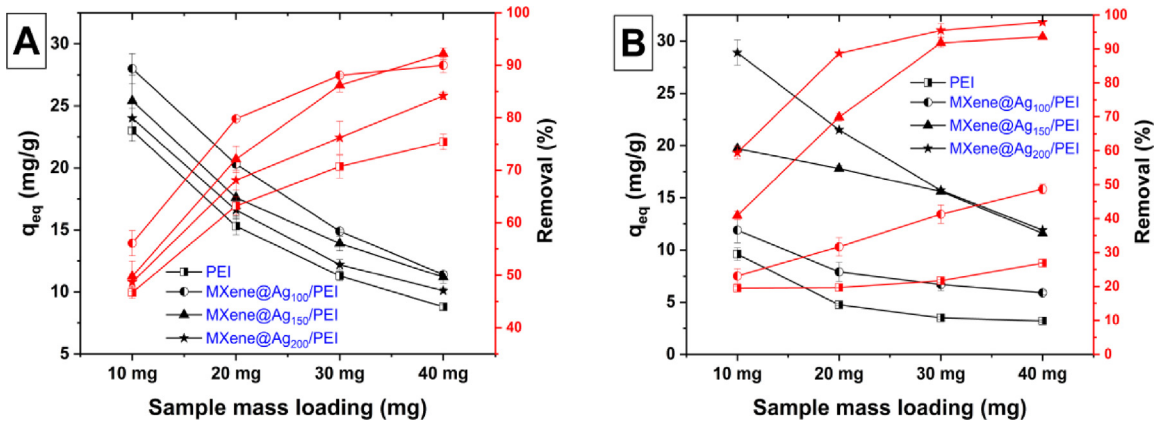

Fig. 8. Removal capacity at equilibrium (right axis) and removal efficiency (left axis) of Hg^{2+} (5 mg/L, 100 mL) with various mass of adsorbents (10–40 mg) from (a) water and (b) river water. Equilibrium time was 180 min in all cases.

by the end of the 90-min kinetics study. Comparing to the water experiments results, the SMX degradation improved possibly due to the presence of sulfates in river water that could have improved the photocatalytic effect by the formation of hydroxyl and sulfate radicals (Kohantorabi et al., 2020). Moreover, there is a clear dependence on adsorbent dosage in photocatalytic degradation of SMX due to the activation of photocatalysts by various radicals that can form in river water under the study conditions, where the highest loading (40 mg) of composite showed the highest degradation rate with maximum C_t/C_0 values of 0.032. These findings allow us to state that even with the presence of high concentrations of cations and anions in natural river water, the MXene@Ag/PEI-based composites serve as effective photocatalysts for SMX degradation.

3.2.4. Influence of co-existing ions on mercury removal

The simultaneous removal of Hg^{2+} from SMX/$HgCl_2$ solutions under light irradiation from DI and river water matrices was also studied to evaluate the influence of light, SMX and co-existing ions on Hg removal. The adsorption of $HgCl_2$ with PEI and Ag-modified adsorbents was dependent on adsorbent dosage, but not on light irradiation. Fig. 8 represents the calculated equilibrium removal capacity (q_{eq}) and removal efficiency (%) for all adsorbents with loading from 10 to 40 mg used for the removal of mercury (5 mg/L, 100 mL) from DI and river water matrices while in Fig. S8a-h shows its kinetics. The results revealed fast adsorption from the start of kinetics by reaching the maximum removal in 10 min showing removal values of 47–75.4% for 10–40 mg of adsorbent dosages for PEI, correspondingly. After that, the adsorption of $HgCl_2$ fluctuated within the standard deviation range but did not display a substantial difference by the end of the kinetics experiment (Fig. S8a). Ag-modified samples MXene@Ag_{100}/PEI and MXene@Ag_{150}/PEI showed noticeably improved removal performance by reaching, on average, removal values of ~56% and 50% for 10 mg, ~80 and 72% for 20 mg, 88 and 86% for 30 mg and 90 and 92% for 40 mg adsorbent dosages, correspondingly (Fig. 8a). It is noticeable that MXene@Ag_{200}/PEI revealed a relatively poor adsorption performance of $HgCl_2$ (a bit higher than pristine PEI) suggesting that the latter two might be the optimum Ag-modified samples under these experimental conditions.

Mercury removal from river water, on the other hand, presented a substantial difference in the adsorption performance of PEI. The removal of $HgCl_2$ in the first 10 min under dark conditions reached the maxima of removal values of only 19.5%, which is almost 4-fold lower than in water. After that 10-min kinetics point, all adsorbent dosages of PEI showed negligible fluctuation. In contrast to PEI, modified adsorbents exhibited complex adsorption performance. In the first 10-min point, 40 mg dosages of MXene@Ag_{150}/PEI and MXene@Ag_{200}/PEI reached the highest removal percentage of almost 50 and 81%, respectively, whereas MXene@Ag_{100}/PEI displayed the lowest value of 40%. Unlike the studies in water, the kinetics profile in river water after the 10-min point further increases by reaching the maxima at the end of the 90-min experiment with the % removal values for MXene@Ag_{150}/PEI at 93.6, 91.8, 69.9, and 40.9% for 40 mg, 30 mg, 20 mg, and 10 mg adsorbent dosages, respectively. MXene@Ag_{200}/PEI demonstrated better removal performance with values of 97.9, 95.5, 88.7, and 59.4% for 40 mg, 30 mg, 20 mg, and 10 mg adsorbent dosages, correspondingly (Fig. 8b). The increase of Hg removal with an increase of silver content in composites could be attributed to the formation of Hg–Ag amalgam as reported elsewhere (Tauanov et al., 2020). It should be noticed that there is a slight dependence on the removal kinetics depending on adsorbent dosage for PEI and comparatively noticeable dependence for MXene@Ag_{100}/PEI, MXene@Ag_{150}/PEI, and MXene@Ag_{200}/PEI with the following trend: 40 mg > 30 mg > 20 m > 10 mg.

In order to evaluate the adsorption kinetics, pseudo-first order and pseudo-second order models were fit to the experimental data (Ho and McKay, 1999):

$$\ln(q_e - q_t) = \ln q_e - k_1 t \tag{3}$$

Table 1
Parameters of kinetic models adjusted to the removal of Hg^{2+} by the synthesized materials.

Matrix	Sample	Pseudo-first order model				Pseudo-second order model		
		q_{eq} exp, mg/g	q_{eq} cal, mg/g	K_1, min^{-1}	R^2	q_{eq} cal, mg/g	K_2, g mg^{-1} min^{-1}	R^2
DI water	PEI	8.8	2.7	0.00069	0.7540	9.9	0.10	0.9981
	MXene@Ag_{100}/PEI	11.4	2.1	0.00045	0.8712	11.9	0.43	0.9999
	MXene@Ag_{150}/PEI	11.2	3.2	0.00067	0.9064	11.9	0.67	0.9999
	MXene@Ag_{200}/PEI	10.1	2.7	0.00059	0.9225	11.5	0.05	0.9977
River water	PEI	3.2	1.4	0.00047	0.4645	3.1	0.17	0.9819
	MXene@Ag_{100}/PEI	5.9	6.7	0.00057	0.7683	11.2	0.2	0.9862
	MXene@Ag_{150}/PEI	11.6	2.7	0.00058	0.9225	11.6	0.28	0.9998
	MXene@Ag_{200}/PEI	11.9	3.7	000151	0.6325	18.7	0.02	0.9901

$$\frac{t}{q_t} = \frac{1}{k_2 q_e^2} + \frac{t}{q_e} \tag{4}$$

where q_e and q_t is the amount (mg/g) of mercury adsorbed at equilibrium and at time t (min), respectively. The pseudo-first-order constant k_1 (min^{-1}) and q_e^{cal} can be obtained from the slope and intercept of the $\ln(q_e - q_t)$ versus t graph. The pseudo-second-order constant k_2 (g mg^{-1} min^{-1}) and q_e^{cal} can be calculated from the t/q_t versus t graph.

Table 1 shows that pseudo second-order kinetics is the model that fits better the experimental results for all samples for both DI and river water. For the pristine PEI cryogel, the model gave an adsorption capacity of 9.9 and 3.1 mg/g against the experimental value of 8.8 and 3.2 mg/g for DI and river water, respectively. In both cases correlation coefficients were high (R^2 is 0.9981 and 0.9819). In the case of MXene@Ag/PEI composites, the calculated q_{eq} were also close to the experimental value with $R^2 > 0.98$ in all samples.

The pseudo second-order kinetics diffusion coefficient (k_2) of PEI is 0.1–0.17 g mg^{-1} min^{-1}, which agrees with the experimental observations of a relatively rapid mercury adsorption. In case of MXene@Ag_{100}/PEI and MXene@Ag_{150}/PEI the k_2 values increase with increase of a silver content probably due to the faster adsorption of mercury ions. Interestingly to note that k_2 for MXene@Ag_{200}/PEI was dramatically lower compared to other composites 0.05 and 0.02 g mg^{-1} min^{-1}. This was possibly due to the partial blocking of macropores of the cryogel by the MXene@Ag_{200} particles, which led to a decrease in diffusion.

The results of adsorption and photocatalytic decomposition reported in Figs. 5–8 and Table 1 indicate the effectivity of the composites for the removal of heavy metals and organic pollutants. The new data achieved, as well as previously published works with other materials (Liu et al., 2020; Yang et al., 2017a), support the sorption and photocatalytic mechanism proposed. The mechanism of adsorption is driven by the interaction of Hg^{2+} with the functional groups of cryogel *via* van der Waals forces, and complexation reactions possibly involving interaction with the F^- and O^- groups of the MXene phase (Baimenov et al., 2020; Othman et al., 2022). As for the mechanisms playing a role in the photodegradation of SMX molecules, the reaction of the organic pollutant with active species O^{2-} and/or ·OH that formed by the photoinduction of the nanomaterials lead to the degradation of the antibiotic. MXene, due to its high electrical conductivity, can facilitate the separation of photoinduced charges (and reduce their recombination) (Zhang et al., 2021a), while the incorporation of AgNPs improves the ability of the photocatalyst to absorb light due to surface plasmon resonance of Ag impelling various photochemical and redox reactions which will degrade SMX (Satheeshkumar et al., 2016; Vu et al., 2020). Overall, the incorporation of MXene@Ag into the structure of cryogels made possible improving the adsorption of mercury ions and also impart photocatalytic properties to the composites.

Conclusion

Polyethylene imine and dimethylacrylamide based cryogel (PEI) were synthesized for the first time. The cryogels were functionalized to MXene@Ag composites that embed single-layer 2D-structured MXenes with deposited Ag nanoparticles. The MXenes were produced via etching of Al from the precursor Ti_3AlC_2 MAX phase, and were subsequently modified with Ag nanoparticles prepared *in situ* with approximate mean particle sizes of 100, 150 and 200 nm. The composite with MXene:$AgNO_3$ ratio of 200 mL MXene colloidal solution:100 mg Ag NMPs, respectively, had the best performance. The resulting PEI cryogels and MXene@Ag/PEI composites were tested for the photo degradation of a main organic contaminant, SMX, and adsorption of Hg^{2+} from spiked distilled and river water matrices. Ag particle size and loading impacted the degradation of the model organic pollutant (SMX). Almost 80% of SMX was removed via photocatalysis in DI water. Interestingly, the removal of SMX assayed river water via photocatalysis of improved to 97% due to the possible generation of secondary radicals that could be involved in the degradation of the antibiotic. In parallel, the adsorption of mercury species from the mixture of SMX/$HgCl_2$ solution showed that the removal of Hg^{2+} with the composite was independent from the co-existing cation and anions in water and reached almost 98% when treating high doses of Hg in water (100 mL 5 mg/L $HgCl_2$ using 40 mg of MXene@Ag_{200}/PEI composite). The mechanism of photocatalysis may have involved surface plasmon resonance of Ag nanoparticles, while MXene, with high electrical conductivity properties, served as a co-catalyst enhancing the photodegradation efficiency. The mercury removal mechanisms involved complexation/chelation and electrostatic interactions of Hg species with functional groups in both PEI and MXene@Ag. Future work should test the removal of these contaminants in water samples of wider water qualities for understanding

better the required structural properties of the composite for its optimal performance. Furthermore, testing the removal of additional emerging contaminants of different chemical nature at environmental concentrations will help to devise the potential universality of the composite proposed for producing drinking water. These results are needed to establish the cost/benefit of preparing and using the composite and will support or discourage its production on a larger scale. The results of this study indicate that the combination of adsorption and photocatalytic properties of 3D-structured cryogel and 2D-structured MXene are an opportunity for effective removal of organic pollutants and metal ions from water of distinct compositions with a single material.

CRediT authorship contribution statement

Harry K. Megbenu: Writing – original draft, Software, Investigation. **Chingis Daulbayev:** Conceptualization, Methodology, Software, Writing – original draft. **Armanbek Nursharip:** Investigation, Validation, Formal analysis. **Zhandos Tauanov:** Writing – original draft, Formal analysis, Methodology. **Stavros Poulopoulos:** Resources, Writing – review & editing. **Rosa Busquets:** Methodology, Formal analysis, Writing – review & editing. **Alzhan Baimenov:** Conceptualization, Methodology, Supervision, Funding acquisition, Writing – review & editing.

Declaration of competing interest

The authors declare that they have no known competing financial interests or personal relationships that could have appeared to influence the work reported in this paper.

Data availability

Data will be made available on request.

Acknowledgments

This work was supported by the Ministry of Science and Higher Education of the Republic of Kazakhstan through the project AP09259907.

Appendix A. Supplementary data

Supplementary material related to this article can be found online at https://doi.org/10.1016/j.eti.2023.103350.

References

Aftab, K., Iqbal, S., Khan, M.R., Busquets, R., Noreen, R., Ahmad, N., Kazimi, S.G.T., Karami, A.M., Al Suliman, N.M.S., Ouladsmane, M., 2023. Wastewater-irrigated vegetables are a significant source of heavy metal contaminants: Toxicity and health risks. Molecules 28, http://dx.doi.org/10.3390/molecules28031371.

Alhabeb, M., Maleski, K., Anasori, B., Lelyukh, P., Clark, L., Sin, S., Gogotsi, Y., 2017. Guidelines for synthesis and processing of two-dimensional titanium carbide (Ti3C2Tx MXene). Chem. Mater. 29, 7633–7644. http://dx.doi.org/10.1021/acs.chemmater.7b02847.

Amiri, M.J., Abedi-Koupai, J., Eslamian, S.S., Arshadi, M., 2016. Adsorption of Pb(II) and Hg(II) ions from aqueous single metal solutions by using surfactant-modified ostrich bone waste. Desalin. Water Treat. 57, 16522–16539. http://dx.doi.org/10.1080/19443994.2015.1079253.

Anasori, B., Lukatskaya, M.R., Gogotsi, Y., 2017. 2D metal carbides and nitrides (MXenes) for energy storage. Nat. Rev. Mater. 2, 16098. http://dx.doi.org/10.1038/natrevmats.2016.98.

Baimenov, A., Berillo, D.A., Poulopoulos, S.G., Inglezakis, V.J., 2020. A review of cryogels synthesis, characterization and applications on the removal of heavy metals from aqueous solutions. Adv. Colloid Interface Sci. 276, 102088. http://dx.doi.org/10.1016/j.cis.2019.102088.

Baimenov, A., Montagnaro, F., Inglezakis, V.J., Balsamo, M., 2022. Experimental and modeling studies of Sr2+and Cs+sorption on cryogels and comparison to commercial adsorbents. Ind. Eng. Chem. Res. 61, 8204–8219. http://dx.doi.org/10.1021/acs.iecr.2c00531.

Borrás, A., Henriques, B., Gonçalves, G., Fraile, J., Pereira, E., López-Periago, A.M., Domingo, C., 2022. Graphene oxide/polyethylenimine aerogels for the removal of Hg(II) from water. Gels 8, http://dx.doi.org/10.3390/gels8070452.

Bruno, R., Mon, M., Escamilla, P., Ferrando-Soria, J., Esposito, E., Fuoco, A., Monteleone, M., Jansen, J.C., Elliani, R., Tagarelli, A., Armentano, D., Pardo, E., 2021. Bioinspired metal-organic frameworks in mixed matrix membranes for efficient static/dynamic removal of mercury from water. Adv. Funct. Mater. 31, 2008499. http://dx.doi.org/10.1002/adfm.202008499.

Chen, F., An, W., Liu, L., Liang, Y., Cui, W., 2017. Highly efficient removal of bisphenol a by a three-dimensional graphene hydrogel-AgBr@rGO exhibiting adsorption/photocatalysis synergy. Appl. Catal. B Environ. 217, 65–80. http://dx.doi.org/10.1016/j.apcatb.2017.05.078.

Choi, K., Lee, S., Park, J.O., Park, J.-A., Cho, S.-H., Lee, S.Y., Lee, J.H., Choi, J.-W., 2018. Chromium removal from aqueous solution by a PEI-silica nanocomposite. Sci. Rep. 8, 1438. http://dx.doi.org/10.1038/s41598-018-20017-9.

Demirci, S., Sahiner, N., 2022. Urease-immobilized PEI cryogels for the enzymatic hydrolysis of urea and carbon dioxide uptake. Ind. Eng. Chem. Res. 61, 2771–2782. http://dx.doi.org/10.1021/acs.iecr.1c05087.

Deng, Y., Tang, L., Zeng, G., Zhu, Z., Yan, M., Zhou, Y., Wang, Jiajia, Liu, Y., Wang, Jingjing, 2017. Insight into highly efficient simultaneous photocatalytic removal of Cr(VI) and 2, 4-diclorophenol under visible light irradiation by phosphorus doped porous ultrathin g-C3N4 nanosheets from aqueous media: Performance and reaction mechanism. Appl. Catal. B Environ. 203, 343–354. http://dx.doi.org/10.1016/j.apcatb.2016.10.046.

Dong, Y., Sang, D., He, C., Sheng, X., Lei, L., 2019. Mxene/alginate composites for lead and copper ion removal from aqueous solutions. RSC Adv. 9, 29015–29022. http://dx.doi.org/10.1039/C9RA05251H.

Dzhardimalieva, G.I., Baimuratova, R.K., Knerelman, E.I., Davydova, G.I., Kudaibergenov, S.E., Kharissova, O.V., Zhinzhilo, V.A., Uflyand, I.E., 2020. Synthesis of copper(II) trimesinate coordination polymer and its use as a sorbent for organic dyes and a precursor for nanostructured material. Polymers (Basel) 12, http://dx.doi.org/10.3390/polym12051024.
Ghosh, S., Othmani, A., Malloum, A., Ke Christ, O., Onyeaka, H., AlKafaas, S.S., Nnaji, N.D., Bornman, C., Al-Sharify, Z.T., Ahmadi, S., Dehghani, M.H., Mubarak, N.M., Tyagi, I., Karri, R.R., Koduru, J.R., Suhas, 2022. Removal of mercury from industrial effluents by adsorption and advanced oxidation processes: A comprehensive review. J. Mol. Liq. 367, 120491. http://dx.doi.org/10.1016/j.molliq.2022.120491.
Halim, J., Cook, K.M., Naguib, M., Eklund, P., Gogotsi, Y., Rosen, J., Barsoum, M.W., 2016. X-ray photoelectron spectroscopy of select multi-layered transition metal carbides (MXenes). Appl. Surf. Sci. 362, 406–417. http://dx.doi.org/10.1016/j.apsusc.2015.11.089.
Ho, Y.S., McKay, G., 1999. Pseudo-second order model for sorption processes. Process. Biochem. 34, 451–465. http://dx.doi.org/10.1016/S0032-9592(98)00112-5.
Hu, T., Zhang, J., Xu, X., Wang, X., Yang, C., Song, C., Wang, S., Zhao, S., 2023. Bioaccumulation and trophic transfer of antibiotics in the aquatic and terrestrial food webs of the yellow River Delta. Chemosphere 323, 138211. http://dx.doi.org/10.1016/j.chemosphere.2023.138211.
Karimi, K.J., Ngumba, E., Ahmad, A., Duse, A.G., Olago, D., Ndwigah, S.N., Mwanthi, M.A., Ayah, R., Dulo, S., 2023. Contamination of groundwater with sulfamethoxazole and antibiotic resistant Escherichia coli in informal settlements in Kisumu, Kenya. PLoS Water 2, 1–15. http://dx.doi.org/10.1371/journal.pwat.0000076.
Kohantorabi, M., Hosseinifard, M., Kazemzadeh, A., 2020. Catalytic activity of a magnetic Fe2O3@CoFe2O4 nanocomposite in peroxymonosulfate activation for norfloxacin removal. New J. Chem. 44, 4185–4198. http://dx.doi.org/10.1039/C9NJ04379A.
Kwon, S.Y., Blum, J.D., Yin, R., Tsui, M.T.-K., Yang, Y.H., Choi, J.W., 2020. Mercury stable isotopes for monitoring the effectiveness of the Minamata convention on mercury. Earth-Sci. Rev. 203, 103111. http://dx.doi.org/10.1016/j.earscirev.2020.103111.
Li, X., Peng, W., Li, L., Chen, S., Ye, L., Peng, C., 2022. Simple synthesis of copper/MXene/polyacrylamide hydrogel catalyst for 4-nitrophenol reduction. Mater. Lett. 324, 132705. http://dx.doi.org/10.1016/j.matlet.2022.132705.
Li, X., Ran, F., Yang, F., Long, J., Shao, L., 2021. Advances in MXene films: Synthesis, assembly, and applications. Trans. Tianjin Univ. 27, 217–247. http://dx.doi.org/10.1007/s12209-021-00282-y.
Liu, W., He, T., Wang, Y., Ning, G., Xu, Z., Chen, X., Hu, X., Wu, Y., Zhao, Y., 2020. Synergistic adsorption-photocatalytic degradation effect and norfloxacin mechanism of ZnO/ZnS@BC under UV-light irradiation. Sci. Rep. 10, 11903. http://dx.doi.org/10.1038/s41598-020-68517-x.
Liu, S.-H., Wei, Y.-S., Lu, J.-S., 2016. Visible-light-driven photodegradation of sulfamethoxazole and methylene blue by Cu2O/rGO photocatalysts. Chemosphere 154, 118–123. http://dx.doi.org/10.1016/j.chemosphere.2016.03.107.
Lozinsky, I.V., 2002. Cryogels on the basis of natural and synthetic polymers: preparation{,} properties and application. Russ. Chem. Rev. 71, 489–511. http://dx.doi.org/10.1070/RC2002v071n06ABEH000720.
Mathis, T.S., Maleski, K., Goad, A., Sarycheva, A., Anayee, M., Foucher, A.C., Hantanasirisakul, K., Shuck, C.E., Stach, E.A., Gogotsi, Y., 2021. Modified MAX phase synthesis for environmentally stable and highly conductive Ti_3 C_2 MXene. ACS Nano 15, 6420–6429. http://dx.doi.org/10.1021/acsnano.0c08357.
Natu, V., Hart, J.L., Sokol, M., Chiang, H., Taheri, M.L., Barsoum, M.W., 2019. Edge capping of 2D-mxene sheets with polyanionic salts to mitigate oxidation in aqueous colloidal suspensions. Angew. Chemie Int. Ed. 58, 12655–12660. http://dx.doi.org/10.1002/anie.201906138.
Oliveira, C., Lima, D.L.D., Silva, C.P., Calisto, V., Otero, M., Esteves, V.I., 2019. Photodegradation of sulfamethoxazole in environmental samples: The role of pH, organic matter and salinity. Sci. Total Environ. 648, 1403–1410. http://dx.doi.org/10.1016/j.scitotenv.2018.08.235.
Othman, Z., Mackey, H.R., Mahmoud, K.A., 2022. A critical overview of mxenes adsorption behavior toward heavy metals. Chemosphere 295, 133849. http://dx.doi.org/10.1016/j.chemosphere.2022.133849.
Parvulescu, V.I., Epron, F., Garcia, H., Granger, P., 2022. Recent progress and prospects in catalytic water treatment. Chem. Rev. 122, 2981–3121. http://dx.doi.org/10.1021/acs.chemrev.1c00527.
Perera, A.S., Melia, P.M., Bristow, R.M.D., McGettrick, J.D., Singer, R.J., Bear, J.C., Busquets, R., 2022. A non-doped microporous titanosilicate for bimodal adsorption-photocatalysis based removal of organic water pollutants. Microporous Mesop. Mater. 345, 112276. http://dx.doi.org/10.1016/j.micromeso.2022.112276.
Privar, Y., Malakhova, I., Pestov, A., Fedorets, A., Azarova, Y., Schwarz, S., Bratskaya, S., 2018. Polyethyleneimine cryogels for metal ions sorption. Chem. Eng. J. 334, 1392–1398. http://dx.doi.org/10.1016/j.cej.2017.11.097.
Saravanakumar, K., Yun, K., Maheskumar, V., Yea, Y., Jagan, G., Park, C.M., 2023. Construction of novel In2S3/Ti3C2 MXene quantum dots/SmFeO3 Z-scheme heterojunctions for efficient photocatalytic removal of sulfamethoxazole and 4-chlorophenol: Degradation pathways and mechanism insights. Chem. Eng. J. 451, 138933. http://dx.doi.org/10.1016/j.cej.2022.138933.
Satheeshkumar, E., Makaryan, T., Melikyan, A., Minassian, H., Gogotsi, Y., Yoshimura, M., 2016. One-step solution processing of Ag, Au and Pd@MXene hybrids for SERS. Sci. Rep. 6, 32049. http://dx.doi.org/10.1038/srep32049.
Shahzad, A., Nawaz, M., Moztahida, M., Jang, J., Tahir, K., Kim, J., Lim, Y., Vassiliadis, V.S., Woo, S.H., Lee, D.S., 2019. Ti3C2Tx MXene core–shell spheres for ultrahigh removal of mercuric ions. Chem. Eng. J. 368, 400–408. http://dx.doi.org/10.1016/j.cej.2019.02.160.
Sheng, Y., Wei, Z., Miao, H., Yao, W., Li, H., Zhu, Y., 2019. Enhanced organic pollutant photodegradation via adsorption/photocatalysis synergy using a 3D g-C3N4/TiO2 free-separation photocatalyst. Chem. Eng. J. 370, 287–294. http://dx.doi.org/10.1016/j.cej.2019.03.197.
Szuplewska, A., Kulpińska, D., Dybko, A., Jastrzębska, A.M., Wojciechowski, T., Rozmysłowska, A., Chudy, M., Grabowska-Jadach, I., Ziemkowska, W., Brzózka, Z., Olszyna, A., 2019. 2D Ti2C (MXene) as a novel highly efficient and selective agent for photothermal therapy. Mater. Sci. Eng. C 98, 874–886. http://dx.doi.org/10.1016/j.msec.2019.01.021.
Tauanov, Z., Lee, J., Inglezakis, V.J., 2020. Mercury reduction and chemisorption on the surface of synthetic zeolite silver nanocomposites: Equilibrium studies and mechanisms. J. Mol. Liq. http://dx.doi.org/10.1016/j.molliq.2020.112825.
Udayachandran Thampy, U.S., Mahesh, A., Sibi, K.S., Jawahar, I.N., Biju, V., 2019. Enhanced photocatalytic activity of ZnO–nio nanocomposites synthesized through a facile sonochemical route. SN Appl. Sci. 1, 1478. http://dx.doi.org/10.1007/s42452-019-1426.
Vu, X.H., Dien, N.D., Ha Pham, T.T., Trang, T.T., Ca, N.X., Tho, P.T., Vinh, N.D., Van Do, P., 2020. The sensitive detection of methylene blue using silver nanodecahedra prepared through a photochemical route. RSC Adv. 10, 38974–38988. http://dx.doi.org/10.1039/D0RA07869G.
Wang, Y., Ma, L., Xu, F., Ren, R., Wang, J., Hou, C., 2022. Ternary ZIF-67/MXene/CNF aerogels for enhanced photocatalytic TBBPA degradation via peroxymonosulfate activation. Carbohydr. Polym. 298, 120100. http://dx.doi.org/10.1016/j.carbpol.2022.120100.
World Health Organization, 2013. Mercury and Health. Geneva.
Wu, Z., Liang, Y., Yuan, X., Zou, D., Fang, J., Jiang, L., zhang, J., Yang, H., Xiao, Z., 2020. MXene Ti3C2 derived Z–scheme photocatalyst of graphene layers anchored TiO2/g–C3N4 for visible light photocatalytic degradation of refractory organic pollutants. Chem. Eng. J. 394, 124921. http://dx.doi.org/10.1016/j.cej.2020.124921.
Xu, L., Wang, G., Ma, F., Zhao, Y., Lu, N., Guo, Y., Yang, X., 2012. Photocatalytic degradation of an aqueous sulfamethoxazole over the metallic silver and Keggin unit codoped titania nanocomposites. Appl. Surf. Sci. 258, 7039–7046. http://dx.doi.org/10.1016/j.apsusc.2012.03.161.
Yadav, S.K., Singh, D.K., Sinha, S., 2016. Adsorptive removal of Hg(II) from synthetic and real aqueous solutions using modified papaya seed. J. Dispers. Sci. Technol. 37, 1613–1622. http://dx.doi.org/10.1080/01932691.2014.930713.
Yang, J., Li, Z., Zhu, H., 2017a. Adsorption and photocatalytic degradation of sulfamethoxazole by a novel composite hydrogel with visible light irradiation. Appl. Catal. B Environ. 217, 603–614. http://dx.doi.org/10.1016/j.apcatb.2017.06.029.

Yang, Y., Ok, Y.S., Kim, K.-H., Kwon, E.E., Tsang, Y.F., 2017b. Occurrences and removal of pharmaceuticals and personal care products (PPCPs) in drinking water and water/sewage treatment plants: A review. Sci. Total Environ. 596–597, 303–320. http://dx.doi.org/10.1016/j.scitotenv.2017.04.102.

Zhang, L., Ma, P., Dai, L., Li, S., Yu, W., Guan, J., 2021a. In situ crystallization and growth of TiO2 nanospheres between mxene layers for improved adsorption and visible light photocatalysis. Catal. Sci. Technol. 11, 3834–3844. http://dx.doi.org/10.1039/D1CY00239B.

Zhang, T., Wang, Z., Yu, S., Guo, X., Ai, C., Tang, X., Chen, H., Lin, J., Zhang, X., Meng, H., 2021b. Effects of pH and temperature on the structure, rheological and gel-forming properties of sugar beet pectins. Food Hydrocol. 116, 106646. http://dx.doi.org/10.1016/j.foodhyd.2021.106646.

Zhou, L., Deng, H., Zhang, W., Gao, Y., 2015. Photodegradation of sulfamethoxazole and photolysis active species in water under Uv-Vis light irradiation. Fresenius Environ. Bull. 24, 1685–1691.

Zhou, Y., Zhang, J., Luo, X., Lin, X., 2014. Adsorption of Hg(II) in aqueous solutions using mercapto-functionalized alkali lignin. J. Appl. Polym. Sci. 131, http://dx.doi.org/10.1002/app.40749.

Zou, G., Zhang, Z., Guo, J., Liu, B., Zhang, Q., Fernandez, C., Peng, Q., 2016. Synthesis of MXene/Ag composites for extraordinary long cycle lifetime lithium storage at high rates. ACS Appl. Mater. Interfaces 8, 22280–22286. http://dx.doi.org/10.1021/acsami.6b08089.